

Analysis of Radiating Plasma
Boundary Layers

L.L. Lengyel

IPP 1/191 September 1981



MAX-PLANCK-INSTITUT FÜR PLASMAPHYSIK

8046 GARCHING BEI MÜNCHEN

MAX-PLANCK-INSTITUT FÜR PLASMAPHYSIK
GARCHING BEI MÜNCHEN

Analysis of Radiating Plasma
Boundary Layers

L.L. Lengyel

IPP 1/191 September 1981

*Die nachstehende Arbeit wurde im Rahmen des Vertrages zwischen dem
Max-Planck-Institut für Plasmaphysik und der Europäischen Atomgemeinschaft über die
Zusammenarbeit auf dem Gebiete der Plasmaphysik durchgeführt.*

Abstract

The equilibrium and stability properties of radiating plasma boundary layers are checked by means of simple analytical and numerical models with some degree of sophistication regarding the radiative characteristics of the atomic species present in the plasma. The objective of these estimates is information on such properties of radiating layers as their thickness, location, temperature, etc., on the magnitude of the energy fluxes that can be removed from the plasma by means of impurity radiation at tolerable impurity levels, and on the stability of such layers.

The main body of this analysis was completed in cooperation with W.S. Goedheer of FOM-Instituut, Jutphaas, in the spring of 1980.

ANALYSIS OF RADIATING PLASMA BOUNDARY LAYERS

L.L. Lengyel,

Max-Planck-Institut für Plasmaphysik, EURATOM Association,
D-8046 Garching, Germany.

Introduction

Transport calculations performed for ZEPHYR and other tokamak devices (see, for example, /1/) have indicated the existence of certain discharge regimes and plasma parameter ranges associated with intense cooling of the outer plasma layer by impurity radiation and with simultaneous reduction of the outwardly directed energy flux carried by plasma particles. The possible formation of such a relatively cold boundary layer between the plasma core and the wall has significant practical implications: slow-down of the energetic CX neutrals emanating from the plasma core, reduction of wall sputtering and impurity influx, etc.. The process may be self-regulating: an increase of the wall sputtering and impurity influx could lead to increased impurity radiation in the boundary layer and thus to enhanced shielding, which would reduce wall sputtering and impurity influx, etc.. The functions envisaged for such a radiating plasma boundary layer are essentially the same as those of a cold gas blanket first proposed by B. Lehnert (see, for example, /2/).

In the present analysis, the equilibrium and stability properties of radiation layers are checked by means of simple analytical and numerical models with some degree of sophistication regarding the radiative properties of the atomic species present in the plasma. In parts of the calculations, advantage has been taken of the numerical programs developed by Goedheer /3/ for computing the

ionization, recombination, and radiation rates of hydrogen species by means of a multi-level atomic model without the usual equilibrium assumptions. The radiation emitted by impurity ions was calculated by assuming corona equilibrium and using the average ion model of Post et al. /4/. The time-dependent numerical programs used in parts of the calculations were generated by W. Schneider with the aid of the program generator described in /5/.

The objective of these calculations and estimates was to obtain information on the properties of radiation layers such as thickness, location, temperature etc., on the magnitude of the energy flux that can be removed from the plasma by means of impurity radiation at tolerable impurity levels, and on the stability of such layers.

1. Conduction-Radiation Balance

In a first approximation, the convective fluxes had been neglected and the local energy balance had been assumed to be given by the asymptotic solution ($t \rightarrow \infty$) of the time-dependent equation

$$(1.1) \quad \frac{\partial}{\partial t}(3n_e T) = \frac{\partial}{\partial x} \left(n_e \chi_e \frac{\partial T}{\partial x} \right) - C n_e n_I P(T)$$

supplemented by the steady-state boundary conditions

$$(1.2) \quad T_{\text{left}} = T_{\text{wall}} \quad , \quad T_{\text{right}} = T_{\text{plasma}} \quad .$$

In the above expressions, T (eV), n_e (cm^{-3}), n_I (cm^{-3}), χ_e (cm^2/s), and P (ergs. cm^3/s) denote, respectively, the plasma temperature, the electron and impurity densities, the thermal conductivity of the electrons, and the radiation loss function characterizing the impurity radiation. The constant multiplier C is given as

$$C = 0.625 \times 10^{12} \text{ eV / ergs.}$$

The function $P(T)$ was calculated in this section by means of the

average ion model (corona equilibrium) of Post et al. /4/. Oxygen, silicon, iron, and tungsten were considered as possible impurities (see Fig. 1). The boundary temperatures were set high enough ($T_w = 10$ eV, $T_{pl} = 10^3$ eV) to allow hydrogen radiation to be neglected. An arbitrary $T(0, x)$ distribution was assumed as initial condition.

If one assumes negligible electron and impurity density variations across the radiating layer (or approximates the respective distributions by the average values of the respective functions) and uses a temperature-corrected Alcator scaling law for χ_e :

$$(1.3) \quad \chi_e = \chi_A \cdot \bar{T}_*^n, \quad \chi_A \left(\frac{\text{cm}^2}{\text{s}} \right) = \frac{6.25 \times 10^{17}}{n_e (\text{cm}^{-3})},$$

$$\bar{T}_* \equiv \frac{\bar{T}}{T_{ref}}, \quad T_{ref} = 0.8 \text{ keV},$$

n being constant, eq. (1.1) reduces to

$$4.8 \times 10^{-12} n_e \frac{\partial \bar{T}}{\partial t} = 10^6 \frac{\partial}{\partial x} \left(\bar{T}_*^n \frac{\partial \bar{T}}{\partial x} \right) - n_e n_i P(\bar{T}).$$

1.1 Asymptotic Solution

The pair of time-independent equations that defines the asymptotic solution of eq. (1.1) can be written as follows:

$$(1.4 a) \quad Q \left(\frac{\text{ergs}}{\text{cm}^2 \cdot \text{s}} \right) = - \frac{n_e \chi_e}{C} \frac{d\bar{T}}{dx},$$

$$(1.4 b) \quad n_e n_i P(\bar{T}) = - \frac{dQ}{dx} = \text{Rad},$$

where Q is the energy flux and 'Rad' represents the power radiated per unit volume. As can readily be seen, eqs. (1.4) reduce to

$$(1.5) \quad \frac{n_e n_I P(T)}{Q} = \frac{C}{n_e \chi_e} \frac{dQ}{dT},$$

the solution of which is given by

$$(1.6 a) \quad Q^2 - Q_w^2 = 2 \frac{n_e n_I}{C} \int_{T_w}^T (n_e \chi_e) P(T) dT.$$

Introducing the notation

$$(1.6 b) \quad \chi_0 f(T) = n_e \chi_e,$$

χ_0 being the temperature-independent part of $n_e \chi_e$, the solution (1.6) may be rewritten as

$$(1.6 c) \quad Q = \left[Q_{pl}^2 - 2 n_e n_I \chi_0 R_T / C \right]^{1/2},$$

$$R_T \equiv \int_T^{T_{pl}} f(T) P(T) dT.$$

In the case of temperature-independent Alcator scaling one has $f(T) = 1$, and a simple expression is obtained for the ratio of the heat fluxes at the left and right boundaries:

$$(1.7) \quad \frac{Q_w}{Q_{pl}} = \left[1 - 2 \frac{n_e n_I \chi_0}{Q_{pl}^2} \frac{R}{C} \right]^{1/2}, \quad R \equiv \int_{T_w}^{T_{pl}} P(T) dT,$$

$\chi_0 / C = 10^6$. As before, the units of T , n , P , and Q are (eV), (cm^{-3}), ($\text{ergs} \cdot \text{cm}^3 / \text{s}$), and ($\text{ergs} / \text{cm}^2 \cdot \text{s}$), respectively. The value of the integral R is shown in Fig. 2 for various species (impurities) as a function of the plasma temperature.

For the case with $n_e = \text{const}$, $n_I = \text{const}$, Goedheer /6/ suggested a simple way of reducing eqs. (1.4) to (1.7): If one defines

$$(1.8 a) \quad Q^* = Q (n_e n_I)^{-1/2},$$

$$x^* = x (n_e n_I)^{+1/2},$$

and assumes $f(T) = 1$, eqs. (1.4) reduce to

$$(1.8 \text{ a}) \quad Q^* = - \frac{\chi_0}{c} \frac{dT}{dx^*}, \quad P(\tau) = - \frac{dQ^*}{dx^*},$$

and the solution (1.7) can be written for any combinations of n_e and n_I as

$$(1.8 \text{ c}) \quad \frac{Q_w}{Q_{pl}} = \left[1 - 2\chi_0 R / c Q_{pl}^{*2} \right]^{1/2}.$$

Equation (1.5) may be used for generating analytical solutions for a number of simple cases. For example, Lackner /7/ has estimated the heat flux along the magnetic field lines in the divertor chamber of a divertor tokamak by assuming $p_e = \text{const} = p_{e0}$, $n_I/n_e = \text{const} = c_I$,

$$(1.9 \text{ a}) \quad \chi_0 = c_{II} \bar{T}_e^{5/2}, \quad Q \left(\frac{\text{ergs}}{\text{cm}^2 \cdot \text{s}} \right) = - \chi_0 \frac{d\bar{T}_e}{dx},$$

and solving eq. (1.5). The solution is given for this case as

$$(1.9 \text{ b}) \quad \begin{aligned} Q^2 - Q_w^2 &= 2c_I c_{II} (n_{e0} \bar{T}_{e0})^2 R_{II}, \\ R_{II} &\equiv \int_{\bar{T}_w}^{\bar{T}} \bar{T}_e^{1/2} P(\bar{T}_e) d\bar{T}_e, \\ c_{II} &= 1.95 \times 10^9 / (Z \cdot \ln \Lambda). \end{aligned}$$

As before, the units of n_e , T_e , and $P(T)$ are (cm^{-3}) , (eV) , and $(\text{ergs} \cdot \text{cm}^3 \cdot \text{s}^{-1})$, respectively. Figure 2a shows the temperature variation of $R_{II}(T)$ for four impurities: oxygen, silicon, iron, and tungsten.

As can readily be seen from eq. (1.7), the radiation flux may be increased (and thus the thermal flux carried by material particles to the wall decreased) by increasing the average or local values of the electron and/or impurity densities, the value of the effective thermal conductivity in the radiation layer, or the value of the integral $R(T)$, i.e. by selecting impurities with higher emissivities.

However, it should be noted that impurities with higher emissive power usually emit at higher temperatures, i.e. the radiation layer becomes shifted towards the center of the plasma.

The maximum flux that can be radiated away (zero flux at the wall, see eq.(1.6)) is given by

$$(1.10) \quad Q_{\max} = \left(2 \chi_0 n_e n_I R_T / c \right)^{1/2}.$$

Once the value of Q_w is known, the thickness of the radiating layer can be determined by means of the integral (see eqs. (1.4) and (1.6)):

$$(1.11) \quad l = \int_{Q_w}^{Q_{pl}} \frac{dQ}{n_e n_I P(T)} = \int_{T_w}^{T_{pl}} \frac{\chi_0 f(T) dT / c}{\sqrt{Q_w^2 + 2 n_e n_I \chi_0 R_T / c}}$$

Figure 3 shows the variation of Q_w/Q_{pl} as a function of Q_{pl} , for $T = 10$ eV, $T_{pl} = 1$ keV, iron impurity with $n_I = 5 \times 10^{10} \text{ cm}^{-3}$, and for two electron densities $n_e = 10^{14}$ and $3 \times 10^{14} \text{ cm}^{-3}$. Simple Alcator scaling with $f(T) = 1$ has been assumed. The numbers displayed along the curves represent the corresponding radiation layer thicknesses (cm).

1.2 Perturbation Analysis

If one assumes that the radiation power $P(T)$ is a function of some power of the temperature, i.e.

$$(1.12) \quad P(T) = \text{const. } T^\alpha, \quad \alpha \equiv d \ln P / d \ln T,$$

and applies a periodic temperature perturbation of the form

$$(1.13) \quad T = T_0 + T_1, \quad T_1 = \hat{T} \exp(\gamma t + i k_x x) \ll T_0$$

to eq. (1.1), the following expression is obtained for the real part of the growth rate γ (n_e and n_I being assumed to be constant and given):

$$(1.14) \quad \gamma_r = -\frac{1}{3n_e} \left\{ \chi_o f(\bar{T}_0) \left[k_x^2 + n \left(\frac{\partial \ln \bar{T}_0}{\partial x} \right)^2 \right] - (n - \alpha) \frac{\rho n_e n_I P(\bar{T}_0)}{\bar{T}_0} \right\}$$

For simple (temperature-independent) Alcator scaling $n \equiv 0$ and this expression reduces to

$$(1.15) \quad \gamma_r = -\frac{\chi_e}{3} \left(k_x^2 + \alpha \frac{\rho n_I P(T)}{\chi_e \bar{T}_0} \right),$$

i.e. the solution is stable at any perturbation wavelength, provided $\alpha > 0$, i.e. the radiation power emitted increases with increasing temperature. (A spontaneous temperature increase is damped by increased radiative losses). This is, however, not always the case (see Fig. 1). As could be expected, if $P(T)$ decreases with increasing temperature, i.e. $\alpha < 0$, the solution becomes unstable for wavelengths exceeding a critical value

$$(1.16) \quad \lambda_{crit} = \left(\frac{\chi_e \bar{T}_0}{|\alpha| C n_I P(\bar{T}_0)} \right)^{1/2}.$$

Since $\alpha P(T)/T = dP/dT$ can be computed for any given radiation loss function $P(T)$, the maximum admissible wavelength is a unique function of the temperature. Figure 4 shows the variation of λ_{crit} with temperature for iron impurity ($n_I = 5 \times 10^{10} \text{ cm}^{-3}$).

This analysis cannot answer the question whether in a realistic boundary layer the wavelength can locally exceed the critical value. The answer is, however, provided by a straightforward numerical solution of the time-dependent problem.

It should be noted, furthermore, that the net effect of a temperature-dependent thermal conductivity cannot be assessed directly from eq. (1.14) (n appears with opposite signs in the second and third terms on the r.h.s.). For any given temperature distribution, computed, for example, by obtaining the asymptotic solution of eq. (1.1), the local growth rate can be calculated at any location inside the boundary layer. We shall return to this question in the next section.

1.3 Effect of Temperature-Dependent Thermal Conductivity

To check the effect of the temperature-dependence of the thermal conductivity and the stability properties of the solutions obtained, the time-dependent equation (1.1) supplemented by the boundary condition (1.2) was solved numerically. The implicit method applied was devised by W.O.Schneider /5/, whose program generator code provided the numerical scheme used in the solution of the given initial-boundary-value problem. It should be noted that eqs. (1.1) and (1.2) uniquely define the temperature distribution. The heat fluxes resulting at the left and right boundaries are properties of the solution. There are, however, two parameters with the help of which $Q_l = Q_w$ and $Q_r = Q_{pl}$ can be adjusted to any desired value: the impurity content or impurity density n_I (or the electron density n_e) and the distance between the right and left boundaries defined as the radiation layer thickness: $l = x_r - x_l$.

In all calculations reported in this section $n_e = 10^{14} \text{ cm}^{-3}$, $T_l = 10 \text{ eV}$, and $T_r = 1 \text{ keV}$, have been assumed, and iron was considered as the only impurity present.

Figure 5 shows typical T , Q , and $P(T)$ distributions for $n_I = 5 \times 10^{10} \text{ cm}^{-3}$ and $n = 0$ (i.e. temperature-independent thermal conductivity, see eq. (1.3)). The results obtained are as follows: $Q_{pl} = 9.2 \text{ W/cm}^2$, $Q_w = 0.88 \times 10^{-2} \text{ W/cm}^2$, and $l = 18.2 \text{ cm}$.

Keeping the same impurity density, we have assumed thermal conductivities directly or inversely proportional to the square-root of the temperature: $n = +0.5$ and $n = -0.5$, respectively. Solutions were obtained to eq. (1.1) without trying to adjust the heat flux on the plasma side to the original (9.2 W/cm^2) value. The $Q_w/Q_{pl} \ll 1$ condition was re-established by changing the $l = x_r - x_l$ value. For the case $n = +0.5$, $Q_{pl} = 6.95 \text{ W/cm}^2$ ($Q_w = 0.03 \text{ W/cm}^2$) and $l = 16.5 \text{ cm}$ were obtained. The respective values obtained for $n = -0.5$ are: $Q_{pl} = 13.7 \text{ W/cm}^2$ ($Q_w = 0.03 \text{ W/cm}^2$) and $l = 24.5 \text{ cm}$. The respective distributions are shown

$$(1.14) \quad \gamma_r = -\frac{1}{3n_e} \left\{ \chi_o f(\bar{T}_0) \left[k_x^2 + n \left(\frac{\partial \ln \bar{T}_0}{\partial x} \right)^2 \right] - (n - \alpha) \frac{C n_e n_I P(\bar{T}_0)}{\bar{T}_0} \right\}$$

For simple (temperature-independent) Alcator scaling $n \equiv 0$ and this expression reduces to

$$(1.15) \quad \gamma_r = -\frac{\chi_e}{3} \left(k_x^2 + \alpha \frac{C n_I P(T)}{\chi_e \bar{T}_0} \right),$$

i.e. the solution is stable at any perturbation wavelength, provided $\alpha > 0$, i.e. the radiation power emitted increases with increasing temperature. (A spontaneous temperature increase is damped by increased radiative losses). This is, however, not always the case (see Fig. 1). As could be expected, if $P(T)$ decreases with increasing temperature, i.e. $\alpha < 0$, the solution becomes unstable for wavelengths exceeding a critical value

$$(1.16) \quad \lambda_{crit} = \left(\frac{\chi_e \bar{T}_0}{|\alpha| C n_I P(\bar{T}_0)} \right)^{1/2}.$$

Since $\alpha P(T)/T = dP/dT$ can be computed for any given radiation loss function $P(T)$, the maximum admissible wavelength is a unique function of the temperature. Figure 4 shows the variation of λ_{crit} with temperature for iron impurity ($n_I = 5 \times 10^{10} \text{ cm}^{-3}$).

This analysis cannot answer the question whether in a realistic boundary layer the wavelength can locally exceed the critical value. The answer is, however, provided by a straightforward numerical solution of the time-dependent problem.

It should be noted, furthermore, that the net effect of a temperature-dependent thermal conductivity cannot be assessed directly from eq. (1.14) (n appears with opposite signs in the second and third terms on the r.h.s.). For any given temperature distribution, computed, for example, by obtaining the asymptotic solution of eq. (1.1), the local growth rate can be calculated at any location inside the boundary layer. We shall return to this question in the next section.

1.3 Effect of Temperature-Dependent Thermal Conductivity

To check the effect of the temperature-dependence of the thermal conductivity and the stability properties of the solutions obtained, the time-dependent equation (1.1) supplemented by the boundary condition (1.2) was solved numerically. The implicit method applied was devised by W.O.Schneider /5/, whose program generator code provided the numerical scheme used in the solution of the given initial-boundary-value problem. It should be noted that eqs. (1.1) and (1.2) uniquely define the temperature distribution. The heat fluxes resulting at the left and right boundaries are properties of the solution. There are, however, two parameters with the help of which $Q_l = Q_w$ and $Q_r = Q_{pl}$ can be adjusted to any desired value: the impurity content or impurity density n_I (or the electron density n_e) and the distance between the right and left boundaries defined as the radiation layer thickness: $l \equiv x_r - x_l$.

In all calculations reported in this section $n_e = 10^{14} \text{ cm}^{-3}$, $T_l = 10 \text{ eV}$, and $T_r = 1 \text{ keV}$, have been assumed, and iron was considered as the only impurity present.

Figure 5 shows typical T , Q , and $P(T)$ distributions for $n_I = 5 \times 10^{10} \text{ cm}^{-3}$ and $n = 0$ (i.e. temperature-independent thermal conductivity, see eq. (1.3)). The results obtained are as follows: $Q_{pl} = 9.2 \text{ W/cm}^2$, $Q_w = 0.88 \times 10^{-2} \text{ W/cm}^2$, and $l = 18.2 \text{ cm}$.

Keeping the same impurity density, we have assumed thermal conductivities directly or inversely proportional to the square-root of the temperature: $n = +0.5$ and $n = -0.5$, respectively. Solutions were obtained to eq. (1.1) without trying to adjust the heat flux on the plasma side to the original (9.2 W/cm^2) value. The $Q_w/Q_{pl} \ll 1$ condition was re-established by changing the $l = x_r - x_l$ value. For the case $n = +0.5$, $Q_{pl} = 6.95 \text{ W/cm}^2$ ($Q_w = 0.03 \text{ W/cm}^2$) and $l = 16.5 \text{ cm}$ were obtained. The respective values obtained for $n = -0.5$ are: $Q_{pl} = 13.7 \text{ W/cm}^2$ ($Q_w = 0.03 \text{ W/cm}^2$) and $l = 24.5 \text{ cm}$. The respective distributions are shown

in Figs. 6 and 7. Hence with $n > 0$ the radiation layer is shifted towards the wall, its thickness is reduced, and the power that can be radiated away is smaller. With $n < 0$ the radiation layer moves away from the wall, it becomes broader, and a larger heat flux can be radiated away.

The interpretation of such behaviour is straightforward: since in these cases the reference temperature appearing in the thermal conductivity (see eq. (1.3)) is larger than the typical temperatures associated with intense iron radiation, $T_{\text{ref}} > T_{\text{rad}}$, the effective thermal conductivity is reduced in the radiation zone if $n > 0$ ($(T_{\text{rad}}/T_{\text{ref}})^n < 1$) and it increases if $n < 0$. Since the thickness of the radiation layer l is proportional to the ratio $Q/\langle \text{Rad} \rangle$ (see eq. (1.11)), l decreases if $n > 0$ and increases if $n < 0$ ($\langle \text{Rad} \rangle$ is not affected by n).

Let us now estimate the impurity contents that are required (with $n \neq 0$) for radiating away the same power as in the $n = 0$ case. As a reference case we consider the case $Q_r = Q_{\text{pl}} = 10 \text{ W/cm}^2$, $Q_w/Q_{\text{pl}} \ll 1$. The solution of eq. (1.1) yields for this case (see Fig. 8): $n_I = 6 \times 10^{10} \text{ cm}^{-3}$, and $l = 16.5 \text{ cm}$ ($Q_w < 0.03 \text{ W/cm}^2$). Considering now the cases with $n = +0.5$ and $n = -0.5$ and adjusting the impurity density n_I and the radiation layer thickness l until $Q_r = Q_{\text{pl}} = 10 \text{ W/cm}^2$ and $Q_w/Q_{\text{pl}} \ll 1$ are reached (as before, $T_w = 10 \text{ eV}$, $T_{\text{pl}} = 10^3 \text{ eV}$) we obtained the following results: with $n = +0.5$, $n_I = 1.06 \times 10^{11} \text{ cm}^{-3}$, $l = 11.5 \text{ cm}$ (Fig. 9), with $n = -0.5$, $n_I = 2. \times 10^{10} \text{ cm}^{-3}$, $l = 31.0 \text{ cm}$ (Fig. 10), i.e. a decrease of the effective thermal conductivity in the radiation layer can be compensated by a larger impurity content, and vice versa. As before, the thickness of the radiation layer is proportional to $Q/\langle \text{Rad} \rangle$ (Q being constant in this case), and the radiation layer is shifted towards the wall if the effective thermal conductivity is reduced.

Although the convergence of the time-dependent solution to a unique asymptotic distribution defined by the time-independent boundary conditions, irrespective of the initial distributions used and of the

occasional localized perturbations applied, is evidence of the stability of the solution, the local growth rate was checked at every mesh point for perturbation wavelengths $5 \text{ mm} < \lambda < 50 \text{ cm}$ by means of eq. (1.14) applied to the asymptotic solution obtained. As expected, the solution was found to be stable (i.e. $\gamma_r < 0$) in all cases discussed, but the damping rate decreases with increasing wavelength. The results also indicate that at long perturbation wavelengths none of the terms appearing in eq. (1.14) can, in general, be neglected.

Note that the above results and conclusions are based on the assumption of $n_e = \text{const}$ and $n_i = \text{const}$ in the radiation layer, and are only valid for impurities for which $T_{\text{rad}} < T_{\text{ref}} = 0.8 \text{ keV}$. Nevertheless, they illustrate the basic trend caused by the possible temperature dependence of the thermal conductivity.

2. Two-Component Steady-State Boundary Layer Model

Since the minimum plasma temperature used in the previous section ($T_{\text{min}} = T_W = 10 \text{ eV}$) is likely too high for modelling temperatures in the immediate neighbourhood of material walls, a second set of calculations has been performed with $T_{\text{min}} = T_W = 1 \text{ eV}$. Since in the temperature range $T < 10 \text{ eV}$ hydrogen radiation may no longer be neglected, the steady-state two-component model of Goedheer /3/ and his computer program have been used in these calculations. The special feature of this model is the detailed treatment of the hydrogen radiation without the usual equilibrium assumptions, and the correspondingly detailed computation of the ionization and recombination rates. The impurity radiation was calculated, as before, with the help of the average ion model of Post et al. /4/. It is realized that this is a rather crude approximation for the impurities in the plasma boundary layer, but the development of a non-equilibrium radiation model with due allowance for all relevant atomic processes characterizing the impurity species was beyond the scope of this analysis.

2.1 Steady-State Distributions

Goedheer's model is defined by the following set of equations /6/:

$$(2.1) \quad \frac{\partial \Gamma_e}{\partial x} = \dot{S}_e, \quad$$

$$(2.2) \quad \frac{\partial n_e}{\partial x} = - \frac{\Gamma_e}{D_{\text{eff}}}, \quad$$

$$(2.3) \quad \frac{\partial p_a}{\partial x} = (\epsilon_{ia} + \epsilon_{ea})(n_e + n_a)\Gamma_e, \quad$$

$$(2.4) \quad \frac{\partial Q}{\partial x} = \text{Rad}, \quad$$

$$(2.5) \quad \frac{\partial T}{\partial x} = \frac{1}{n_e \chi_{\text{eff}}} \left[Q + \left(\frac{5}{2} kT + E_i \right) \Gamma_e \right],$$

where subscripts e and a refer to electrons and neutral atoms, respectively, $\text{Rad} = \text{Rad}_H + \text{Rad}_I$ represents the total radiation losses (hydrogen and impurities), \dot{S}_e is the net ionization (or recombination) rate, χ_{eff} and D_{eff} represent the effective thermal conductivity and diffusivity, respectively, ϵ is the momentum transfer rate by elastic collisions, and $n_a = p_a/kT$. Under the steady-state conditions assumed the electron and neutral particle fluxes are equal and opposite: $\Gamma_a = -\Gamma_e$. The coordinate x is measured from the wall towards the plasma center. Q represents the heat flux towards the wall. For the transport coefficients χ_{eff} and D_{eff} expressions of the form

$$\chi_{\text{eff}} = \frac{b \chi_g \chi_A}{\chi_A + b \cdot \chi_g}, \quad D_{\text{eff}} = \frac{b D_g \cdot D_A}{D_A + b \cdot D_g},$$

have been used

(subscripts A and B: Alcator and Bohm, b is a constant multiplier equal to 1 or 5). The possibility of temperature-dependent transport coefficients was not considered in this analysis.

Equations (2.1) to (2.5) are supplemented by the following boundary conditions (the integration - a fourth-order Runge-Kutta procedure - starts at the wall):

$$(2.6) \quad \Gamma_e = \Gamma_{ew} < 0 ,$$

$$(2.7) \quad M_e = M_{ew} > 0 ,$$

$$(2.8) \quad p_a = p_{aw} > 0 ,$$

$$(2.9) \quad Q = Q_w \approx 0 ,$$

$$(2.10) \quad T = T_w > 0 .$$

If it is assumed that in the immediate neighbourhood of the wall recombination dominates over ionization (i.e. $\dot{S}_{ew} < 0$), and the temperature is a monotonically increasing function of x , the qualitative description of the solution described by the above set of equations is straightforward /6/:

Since practically all neutral atoms get ionized in the boundary layer, \dot{S}_e first increases, reaches a positive maximum and then reduces to zero (see Fig. 11a). The behaviour of \dot{S}_e defines the variation of the electron flux Γ_e (see eq. (2.1) and Fig. 11b). Hence it follows from eqs. (2.2) to (2.5) that the distributions of n_e , p_a , n_a , etc., must be of the form shown in Fig. 11. The coordinates

x_1 and x_2 denote the boundaries of the recombination zone and the penetration depth (ionization length) of the neutral gas, respectively. The exact forms of the $T(x)$ and $Q(x)$ distributions depend upon the details of the n_a , n_e , Γ_e , and T distributions.

Since the values of the temperature, electron density, and the heat flux on the plasma side are rendered by the solution, the left-hand-side (wall) boundary values are iterated as long as the desired (plasma) conditions are obtained on the right-hand side. A physically plausible solution must display the following property: the neutral particle flux $\Gamma_e = -\Gamma_a$ must become reduced to zero at the same coordinate x_2 at which full ionization is reached (i.e. $\dot{S}_e(x_2) = 0$; the residual neutral density is determined there by the local equilibrium conditions).

Figures 12a and 12b show typical distribution obtained for the following set of parameters:

$$T_w = 1 \text{ eV}$$

$$T_{pl} = 10^3 \text{ eV}$$

$$n_{aw} = 10^{12} \text{ cm}^{-3}$$

$$n_{ew} = 5 \times 10^{13} \text{ cm}^{-3}$$

$$\Gamma_{aw} = 2 \times 10^{16} \text{ cm}^{-2}$$

$$B = 9 \text{ tesla.}$$

Figure 12a corresponds to $n_{Fe} = 2.5 \times 10^{10} \text{ cm}^{-3}$, $n_{ox} = 0$, Fig. 12b to $n_{Fe} = 2.5 \times 10^{10} \text{ cm}^{-3}$, $n_{ox} = 5 \times 10^{11} \text{ cm}^{-3}$ (constant impurity densities were assumed for the whole region considered). The local stopping length of charge exchange neutrals having (or produced at) a temperature three times as high as the local thermal plasma temperature is shown in these figures by straight lines. As can be seen, the presence of oxygen (an impurity with low radiation temperature compared with iron) shifts the radiation layer towards the wall. Such a situation may be undesirable from the point of view of the cx-neutral-wall interaction (see Fig. 12b).

2.2 Stability of the Two-Component Boundary Layer

To obtain a crude idea regarding the stability properties of the solutions described in sec. 2.1, the following assumptions were made: (a) $n_a \ll n_e$, (b) $\partial \ln \Gamma / \partial x \gg \partial \ln \bar{T} / \partial x$, and thus $\partial(\Gamma k \bar{T}) / \partial x \approx k \bar{T} \partial \Gamma / \partial x$ (see Figs. 12 and 13). Introducing an effective diffusion coefficient also for the neutral particles, the time-dependent version of eqs. (2.1) to (2.5) can thus be written in the following form (constant transport coefficient approximation):

$$(2.11) \quad \frac{\partial n_e}{\partial t} - D_e \frac{\partial^2 n_e}{\partial x^2} - \dot{S}_e = 0$$

$$(2.12) \quad \frac{\partial n_a}{\partial t} - D_a \frac{\partial^2 n_a}{\partial x^2} + \dot{S}_e = 0$$

$$(2.13) \quad \frac{\partial}{\partial t} (3 n_e k \bar{T}_e) + E_i \dot{S}_e - \chi n_e \frac{\partial^2 k \bar{T}}{\partial x^2} - \left(D_a \frac{\partial^2 n_a}{\partial x^2} + 2 D_e \frac{\partial^2 n_e}{\partial x^2} \right) \left(\frac{5}{2} k \bar{T} \right) + \text{Rad} = 0$$

Assuming now that $\text{Rad} = \text{const.}$ T^α and $\dot{S}_e = \text{const.}$ T^β , i.e.

$\alpha \equiv d \ln \text{Rad} / d \ln T$, $\beta \equiv d \ln \dot{S}_e / d \ln T$, and applying a linear perturbation to equations (2.11) to (2.13) of the type

$$f = f_0 + f_1, \quad f_1 = \hat{f} \exp(\gamma t + i k_x x) \ll f_0,$$

the following third-order equation is obtained for the growth rate γ :

$$(2.14) \quad \left\{ 3 k m_{e0} \right\} \gamma^3 + \left\{ \left[\chi + 3 n_{e0} (D_a + D_e) \right] k k_x^2 + \right. \\ \left. \left(\frac{5}{2} + 3 \beta \right) k \dot{S}_{e0} + \left(\alpha \cdot \text{Rad}_0 + \beta E_i \dot{S}_{e0} \right) / T_0 \right\} \gamma^2 + \\ \left\{ \left[3 n_{e0} D_a D_e + (D_a + D_e) \chi \right] k k_x^4 + \left[5 \left(\beta + \frac{1}{2} \right) k D_e \dot{S}_{e0} + \right. \right. \\ \left. \left. \frac{1}{2} \left(\beta + 5 \right) k D_a \dot{S}_{e0} + (D_a + D_e) \left(\alpha \cdot \text{Rad}_0 + \beta E_i \dot{S}_{e0} \right) / T_0 \right] k_x^2 \right\} \gamma \\ + D_a D_e k \chi k_x^6 + \left[\frac{5}{2} (1 + \beta) k \dot{S}_{e0} + \left(\alpha \cdot \text{Rad}_0 + \beta E_i \dot{S}_{e0} \right) / T_0 \right] D_a D_e k_x^4 = 0.$$

Once a steady-state solution is given, the local values of α , β , and $D_a = -D_e (\partial n_e / \partial x) / (\partial n_a / \partial x)$ can be computed from the given distributions, and the growth rate γ can be determined at every mesh point as a function of the perturbation wavelength $\lambda = 1/k_x$.

As an example, the distributions corresponding to $c_{ox} = 10^2$ in Fig. 12 are reproduced in Fig. 13 in log-log scales. In addition, the variation of the radiation power is also shown in this figure. A comparison of this curve with the $P(T)$ curves given in Figs. (5) and (10) shows the effect of the particle fluxes and hydrogen radiation in the immediate neighbourhood of the wall. The growth rate computed by means of eq. (2.14) is also shown. As can readily be seen, the solution may be unstable at certain stations. It is noteworthy that the unstable regions coincide with the regions in which the total radiation power decreases with increasing temperature, i.e. the radiation effect also dominates in this case (see the results of sec. 1.2, obtained in the framework of a much simpler approximation). The wavelengths characterizing the maximum growth rates are in the cm range. The questions whether perturbations of such wavelengths can indeed develop in a realistic boundary layer and whether or not the boundary layer remains stable can only be answered on the basis of the solution of the full set of time-dependent equations (see, for example, sec. 1.3). These calculations are yet to be performed.

Fig. 13. Radiation loss function computed for tungsten, iron, silicon, and oxygen by assuming coronal equilibrium [4].

- /1/ J.Neuhauser, K.Borrass, K.Lackner, L.Lengyel, W.Schneider, R.Wunderlich, "Existence and dynamics of a radiation layer near the edge of a fusion plasma", Bull.Am.Phys.Soc. 25 (1980), 1039
- /2/ See, for example, B.Lehnert, "Screening of a plasma from neutral gas penetration", Nucl. Fusion 8 (1968), 173-181; or "Plasma neutral gas boundary layers", Nucl. Instr. Meth. 129 (1975), 31-37
- /3/ W.J.Goedheer, "Models for a steady-state plasma in a gas blanket", Ph.D.Thesis, Univ. of Utrecht, 1978
- /4/ D.E.Post, R.V.Jensen, C.B.Tarter, W.H.Grasberger, W.A.Lokke, "Steady-state radiative cooling rates for low-density, high-temperature plasma", Atomic Data and Nucl.Data Tables 20 (1977), 397-439
- /5/ D.Düchs, W.O.Schneider, "DEQTRAN - a program generator for the solution of 1 D systems of partial differential equations", Proc. 2nd Europ.Conf. on Comp.Physics, Max-Planck-Institut für Plasma Physik, Garching, April 1976
- /6/ Contribution of W.J.Goedheer (IPP guest, March 1980)
- /7/ K.Lackner, private communication

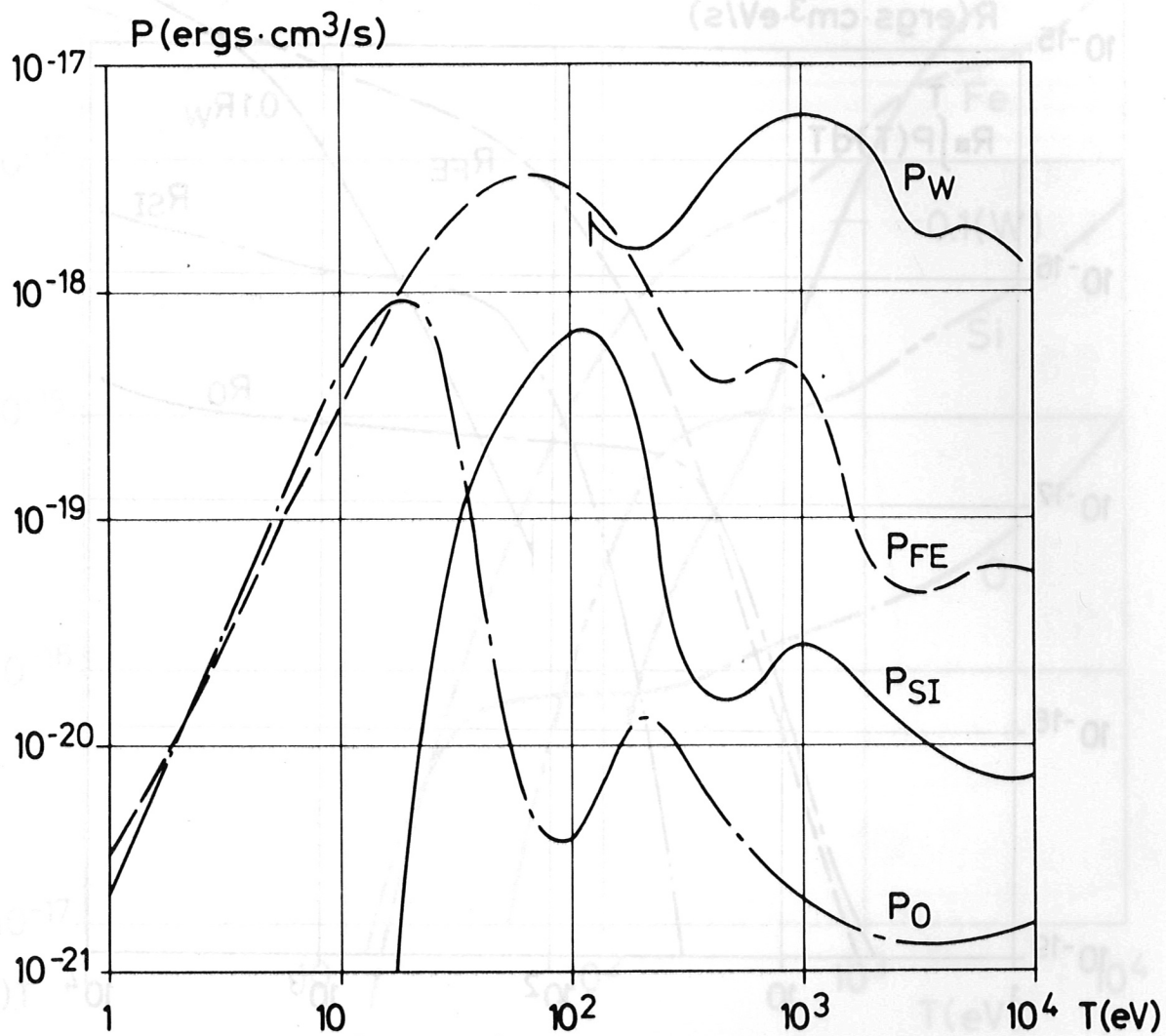


Fig.1: Radiation loss function computed for tungsten, iron, silicium, and oxygen by assuming corona equilibrium /4/.

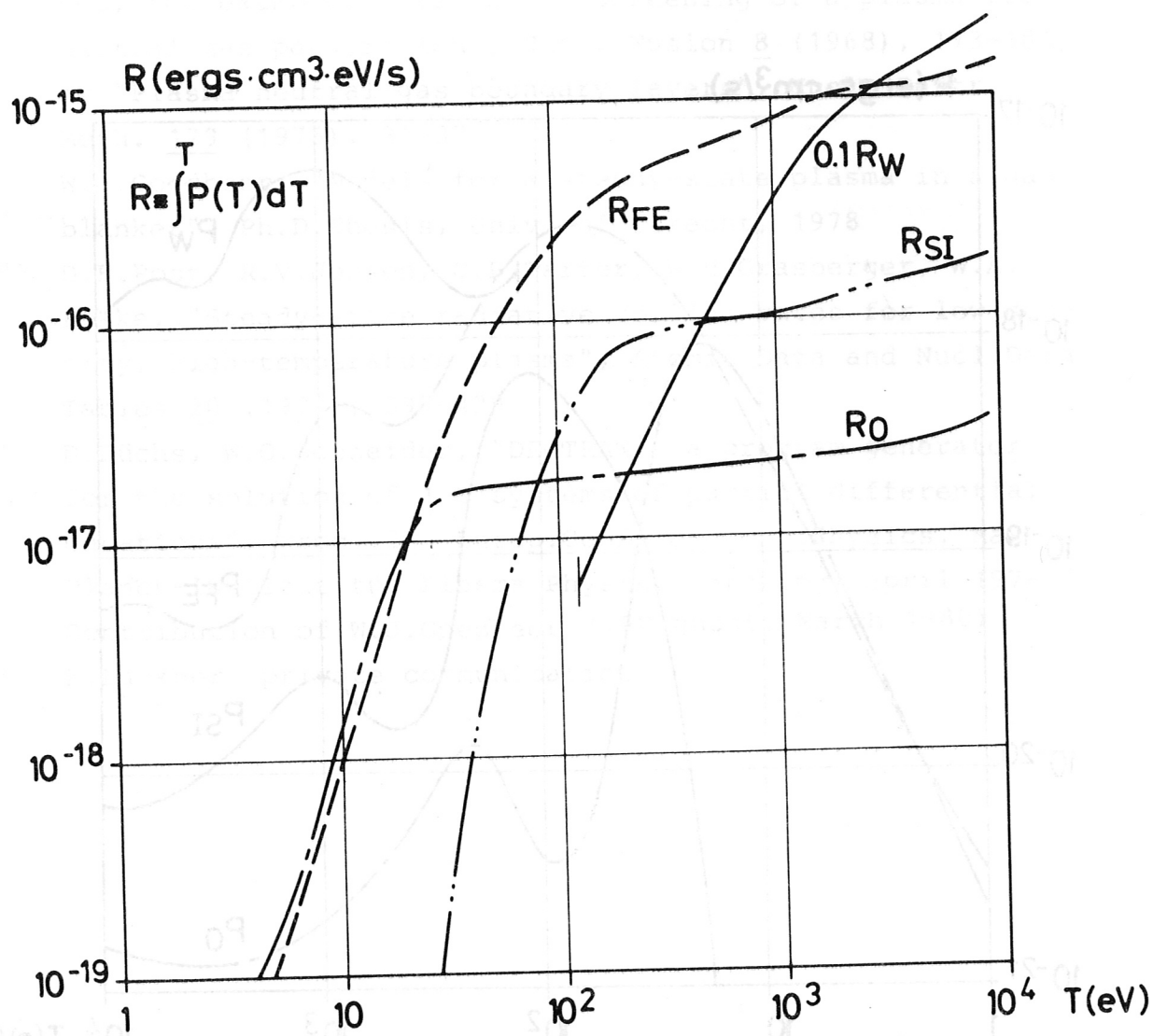


Fig. 2: Loss function integrals computed for the elements referred to in Figure 1.

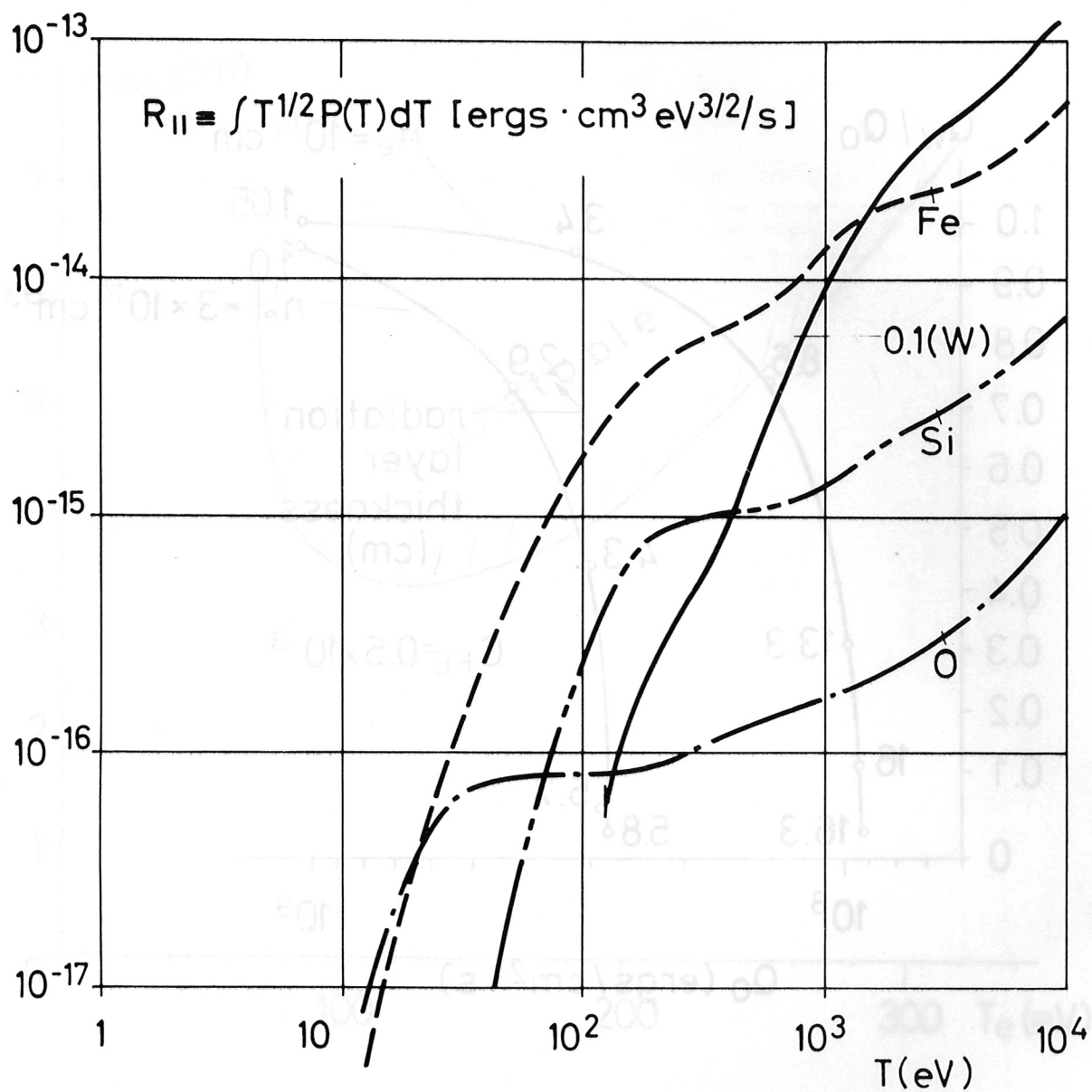


Fig. 2a: Weighted loss function integrals corresponding to constant plasma pressure and $\chi \propto T^{5/2}$ for elements referred to in Figure 1.

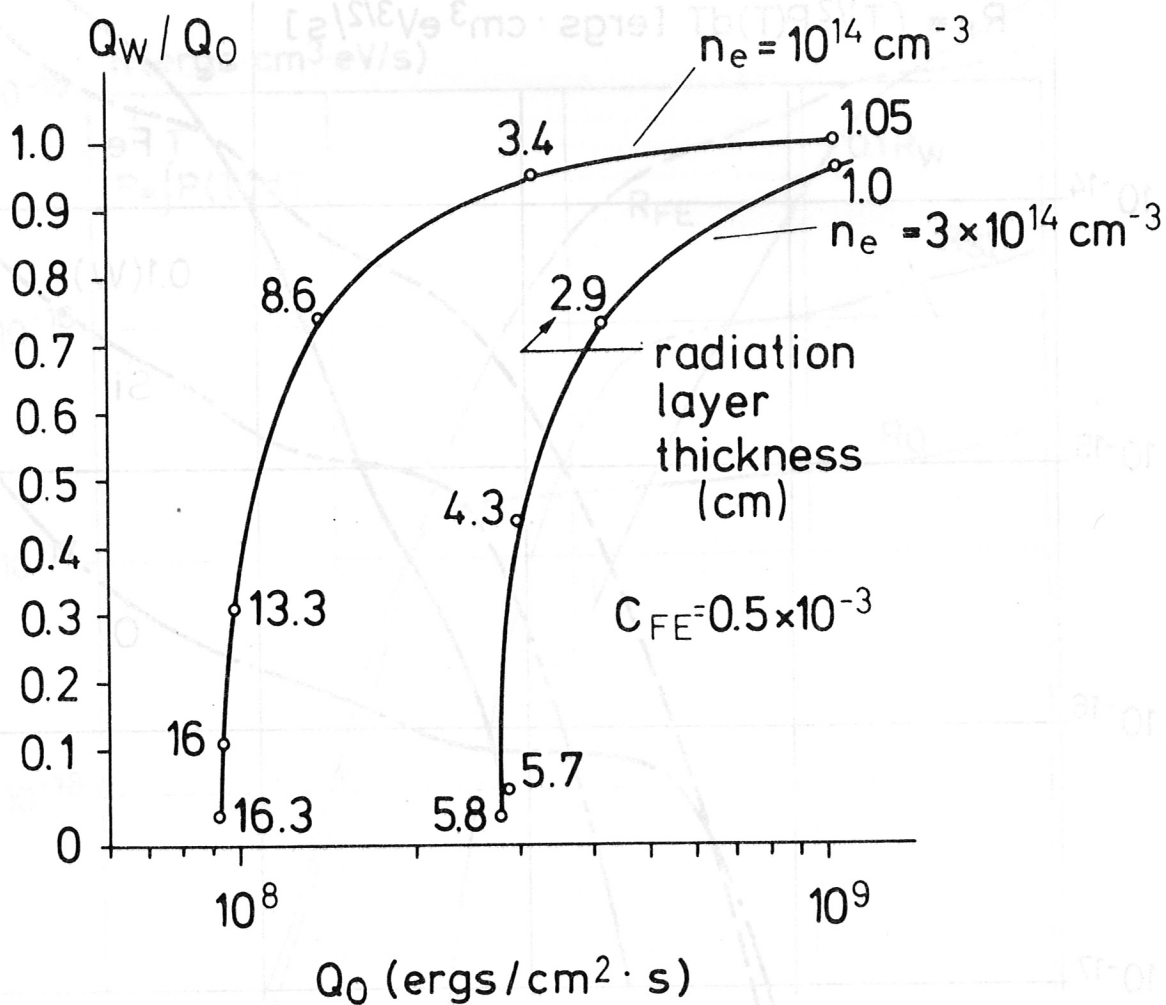


Fig. 3: Conductive heat flux at the wall as a function of the heat flux in the central plasma region computed for hydrogen with iron impurity present ($T_w = 10$ eV, $T_{pl} = 1$ keV).

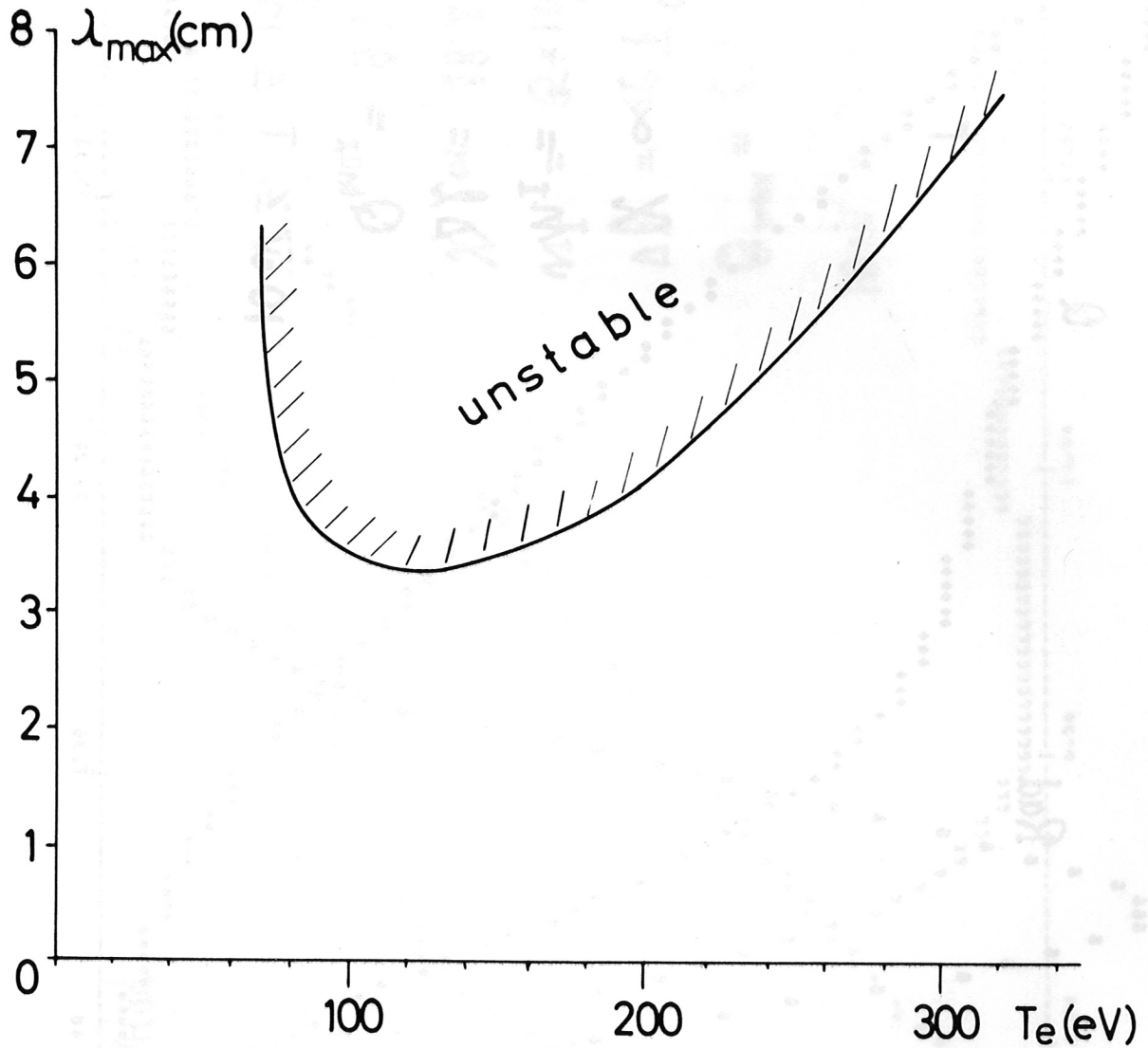


Fig. 4: Critical perturbation wave length as a function of temperature for a radiating hydrogen plasma layer with iron impurity present.

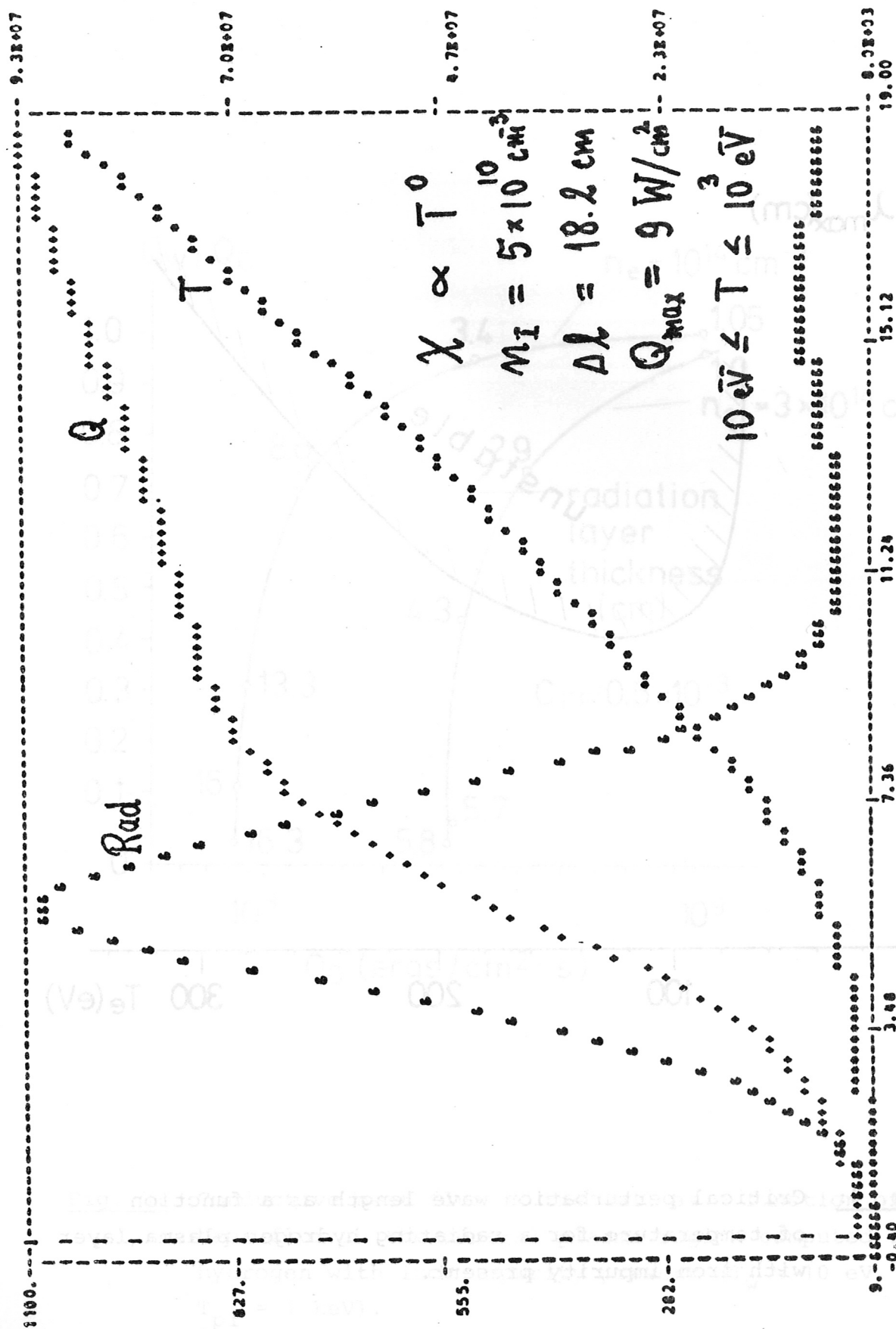


Fig. 5: Distributions of T, Q, and P for a hydrogen plasma with $c_{\text{FE}} = 5 \times 10^{-4}$ and $\chi \propto T^0$.

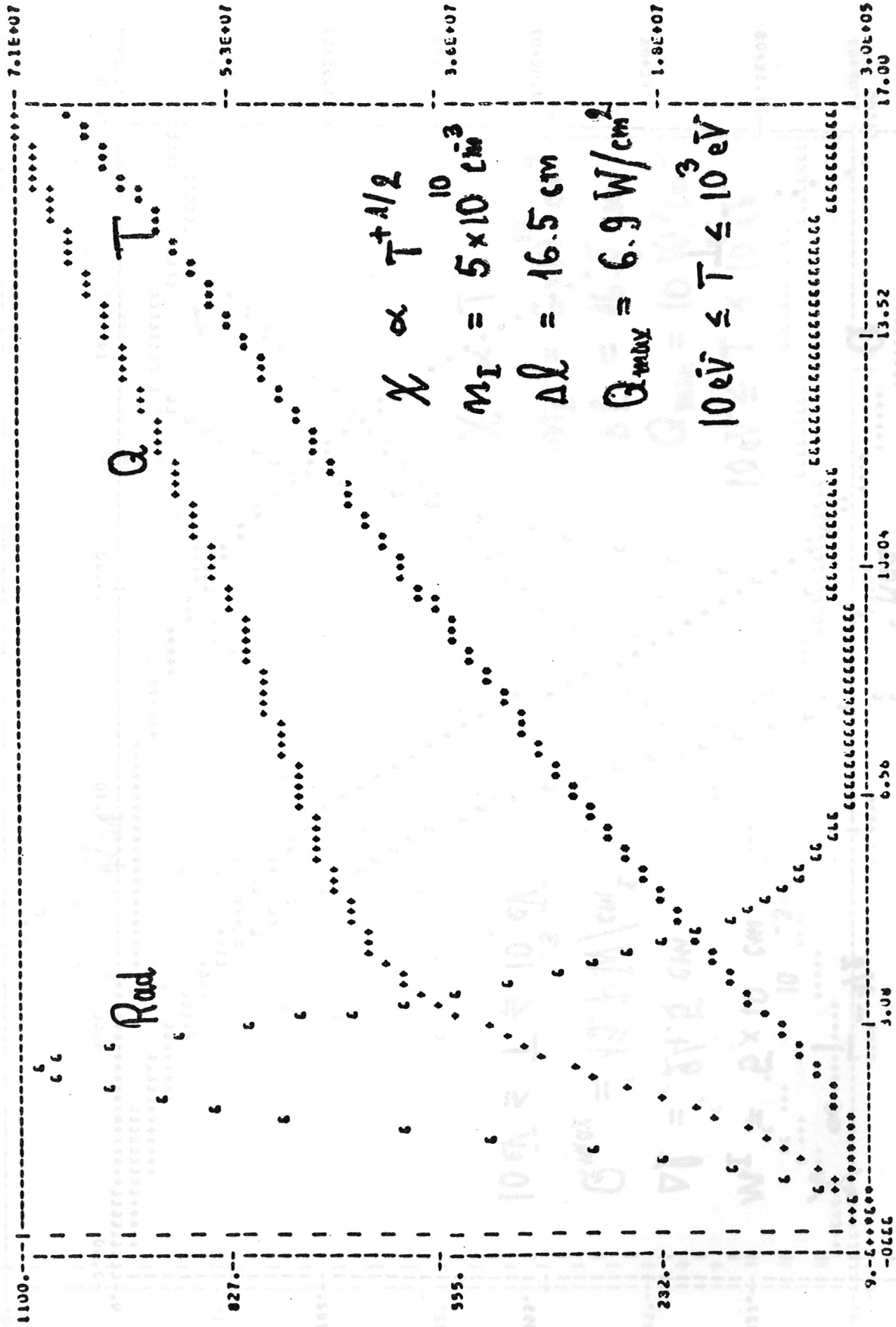


Fig. 6: Distributions of T, Q, and P for a hydrogen plasma with $c_{FE} = 5 \times 10^{-4}$ and $\chi \propto T^{1/2}$.

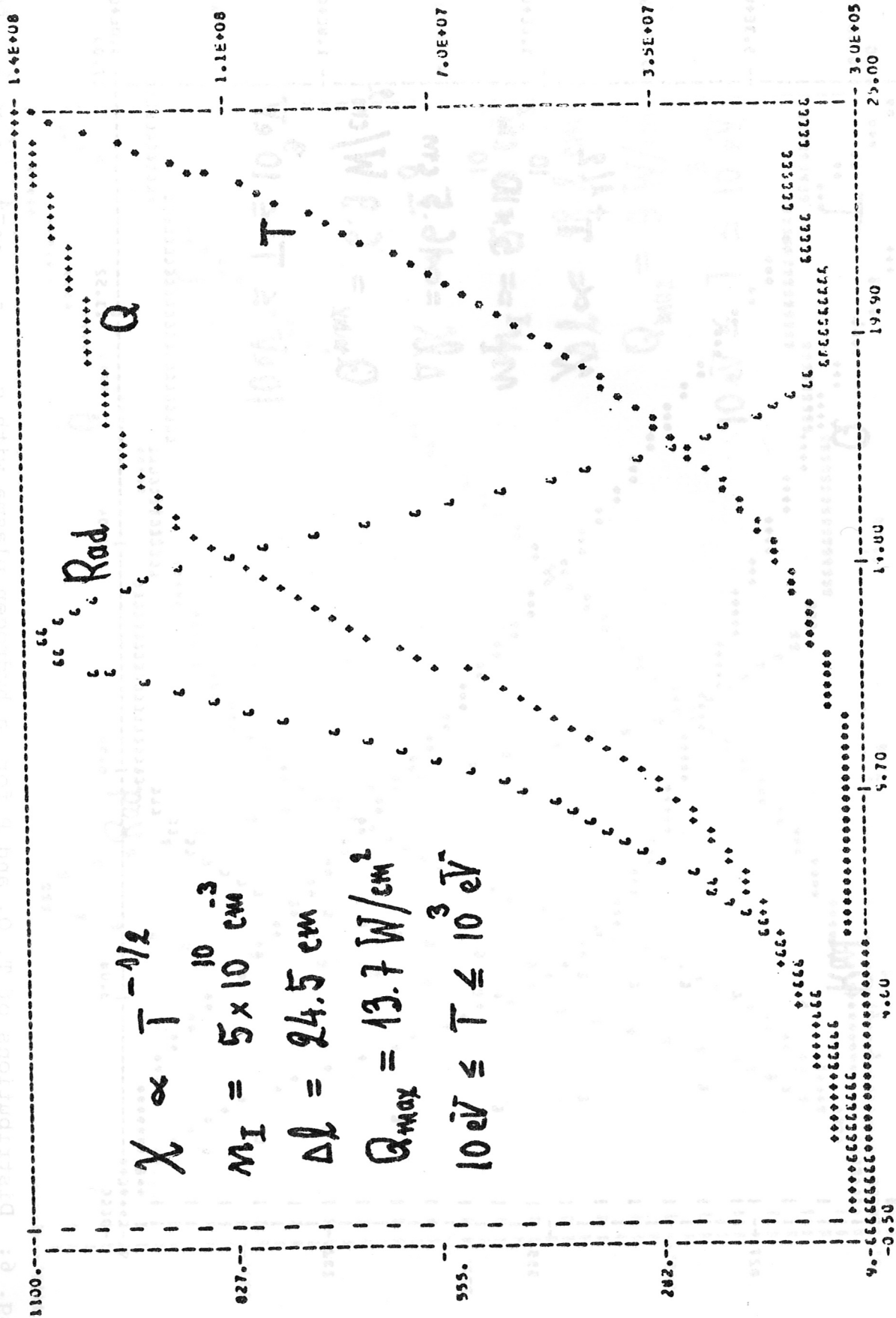


Fig. 7: Distributions of T, Q, and P for a hydrogen plasma with $c_{FE} = 5 \times 10^{-4}$ and $\chi \propto T^{-1/2}$.

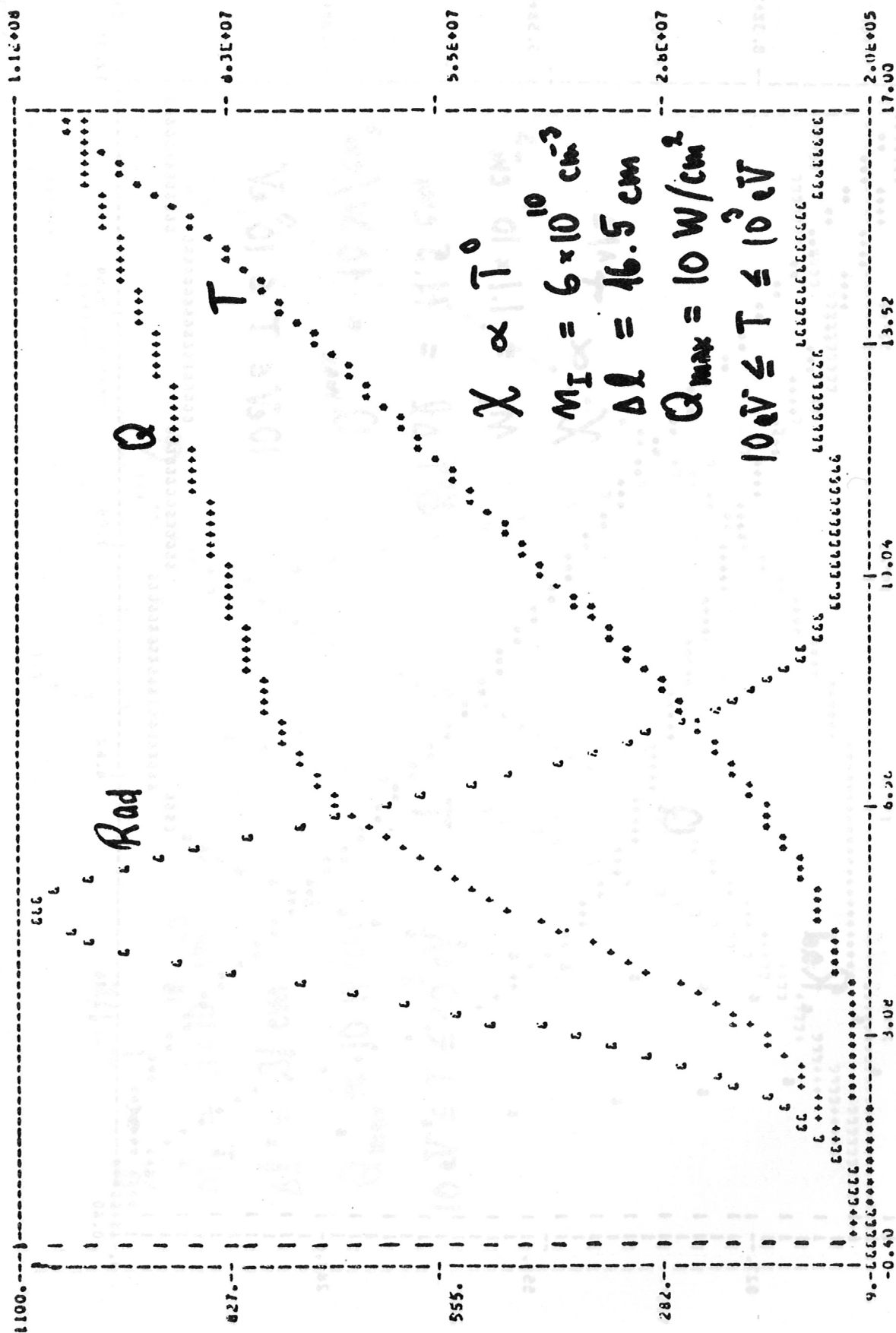


Fig. 8: Distributions of T, Q, and P for a hydrogen plasma with $Q_{pl} = 10 \text{ W/cm}^2$ and $\chi \propto T^0$.

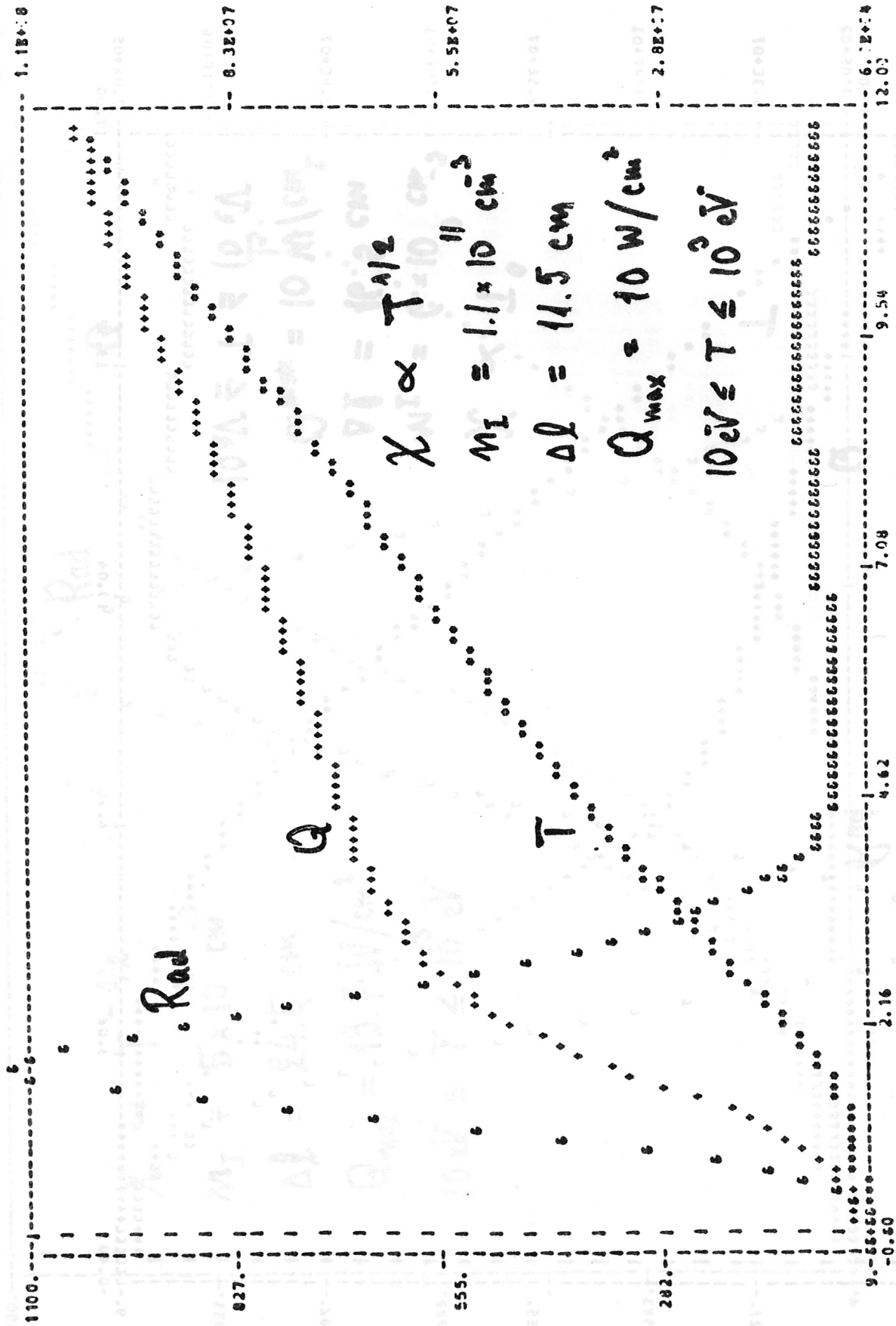


Fig. 9: Distributions of T, Q, and P for a hydrogen plasma with $Q_{pl} = 10 \text{ W/cm}^2$ and $\chi \propto T^{1/2}$.

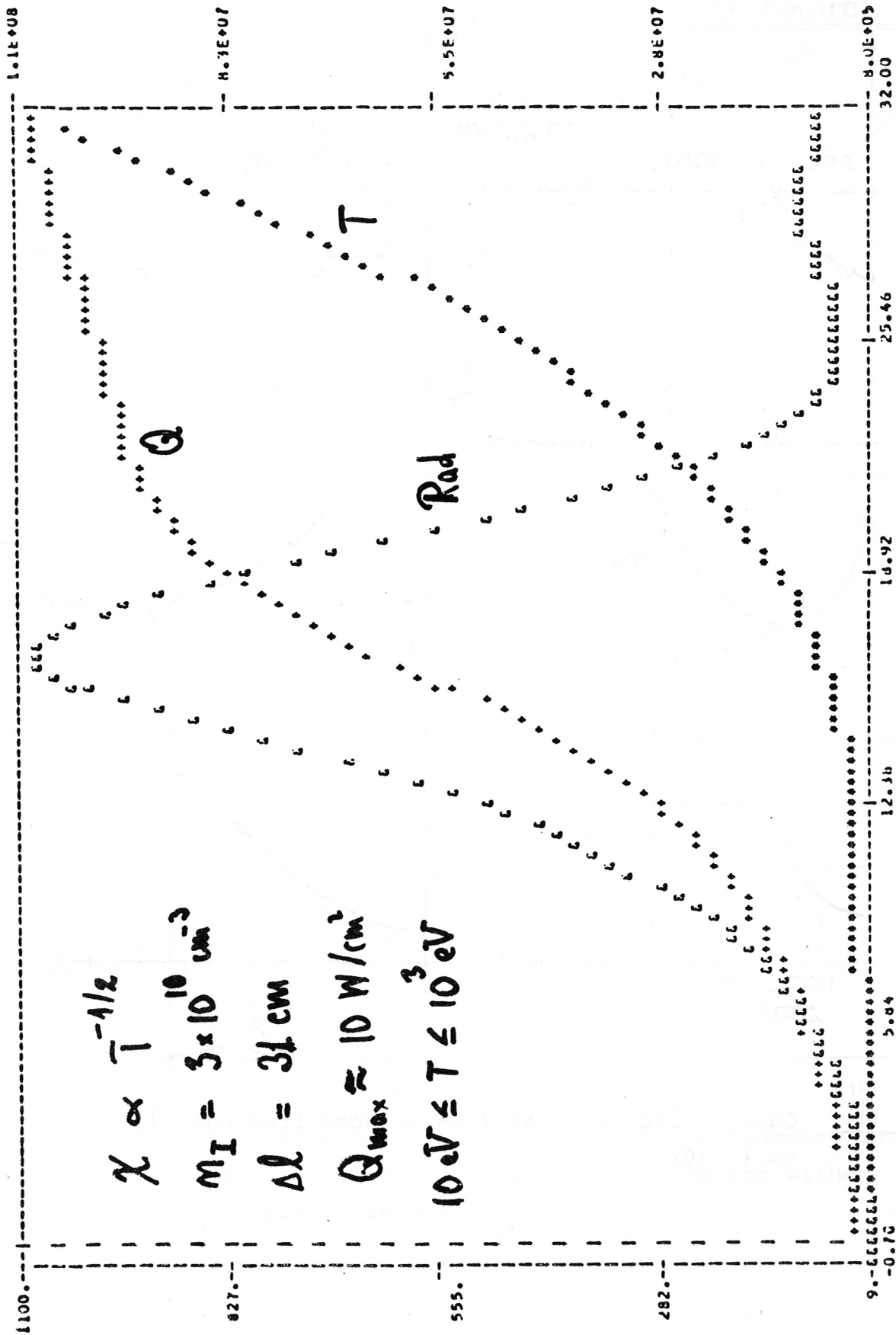


Fig. 10: Distributions of T, Q, and P for a hydrogen plasma with $Q_{pl} = 10 \text{ W/cm}^2$ and $\chi \propto T^{-1/2}$.

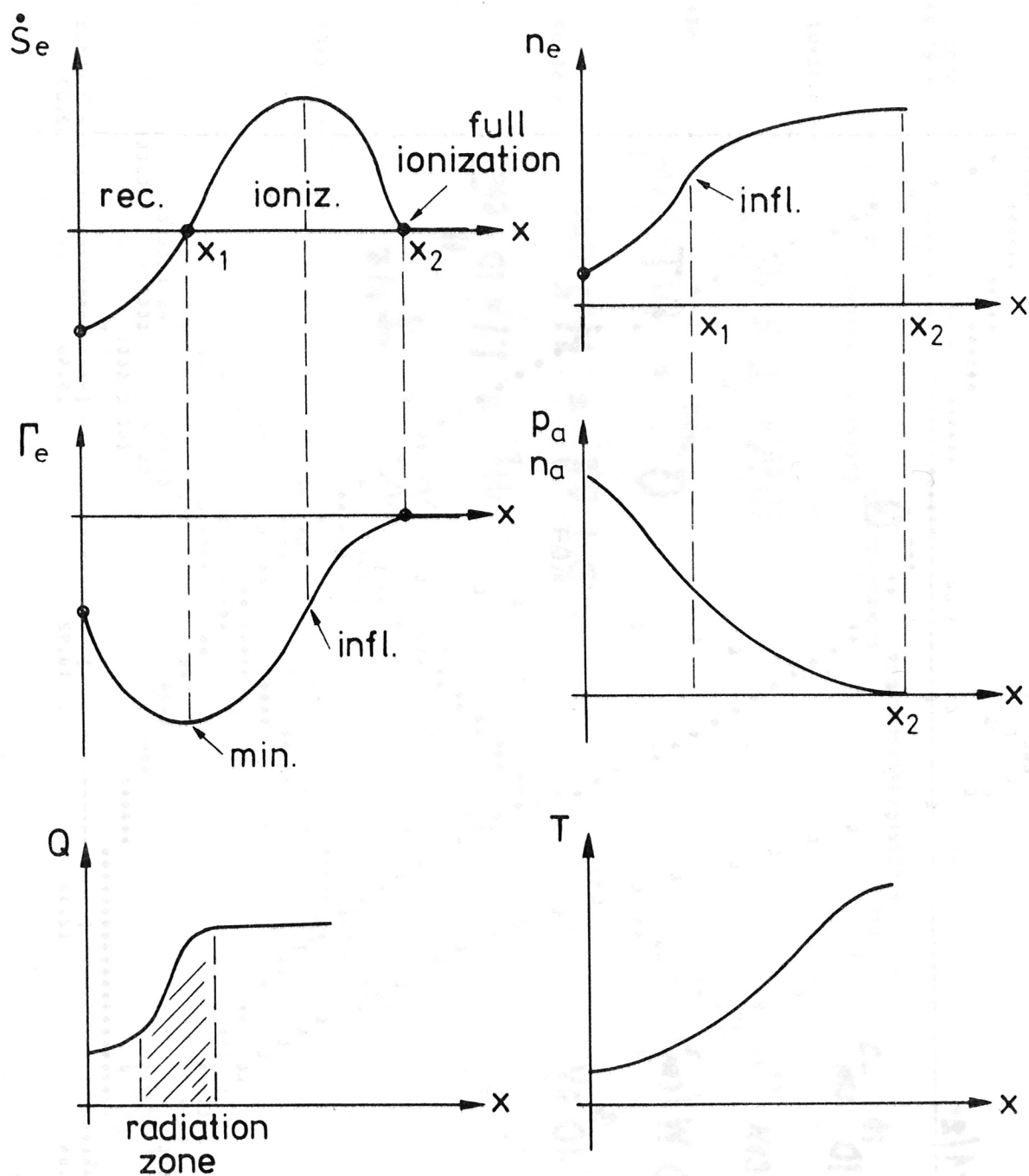


Fig. 11: Qualitative distributions deduced from eqs. (2.1) to (2.10).

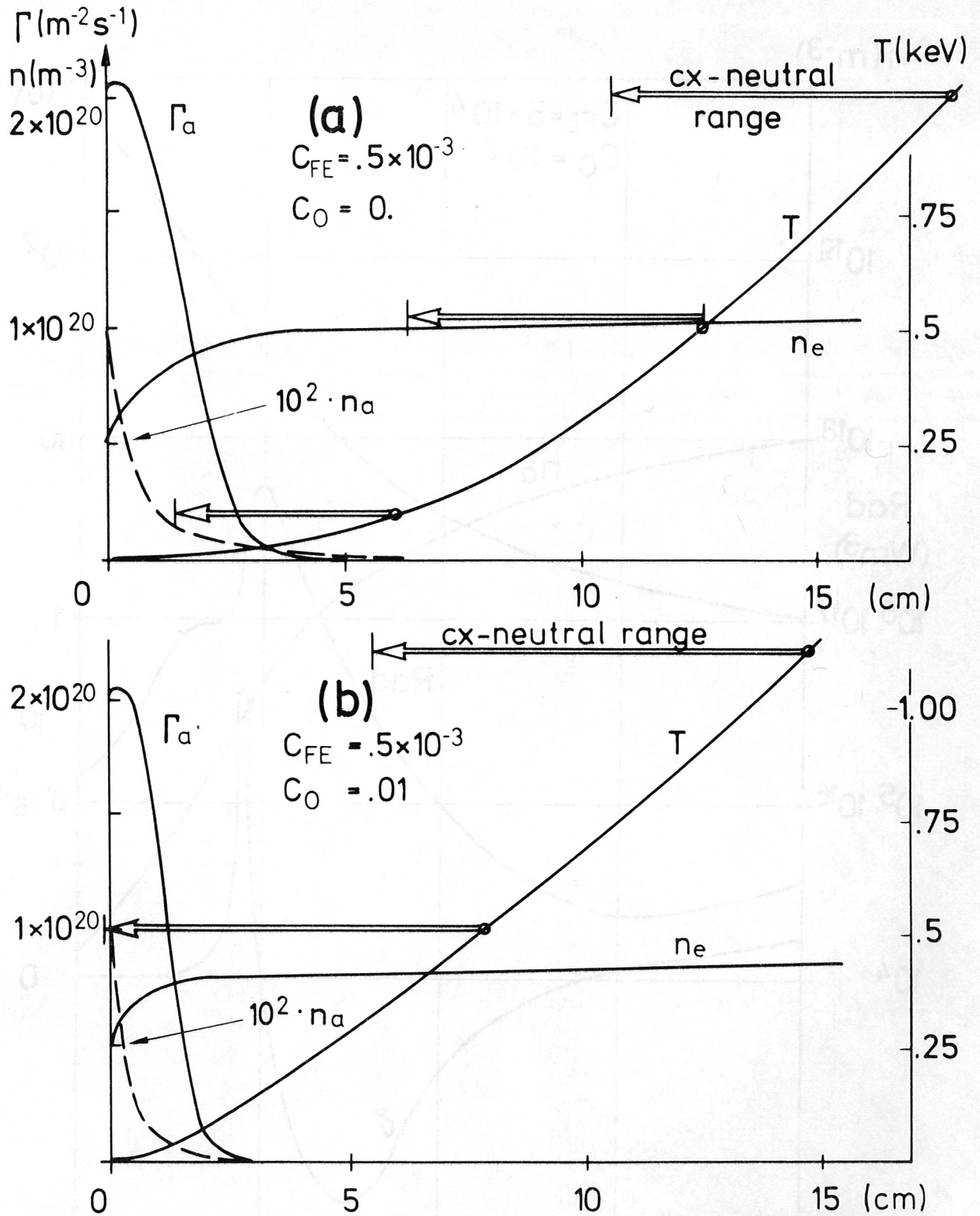


Fig. 12: Parameter distributions in a plasma boundary layer with neutral gas and iron impurity (with and without oxygen impurity) present.

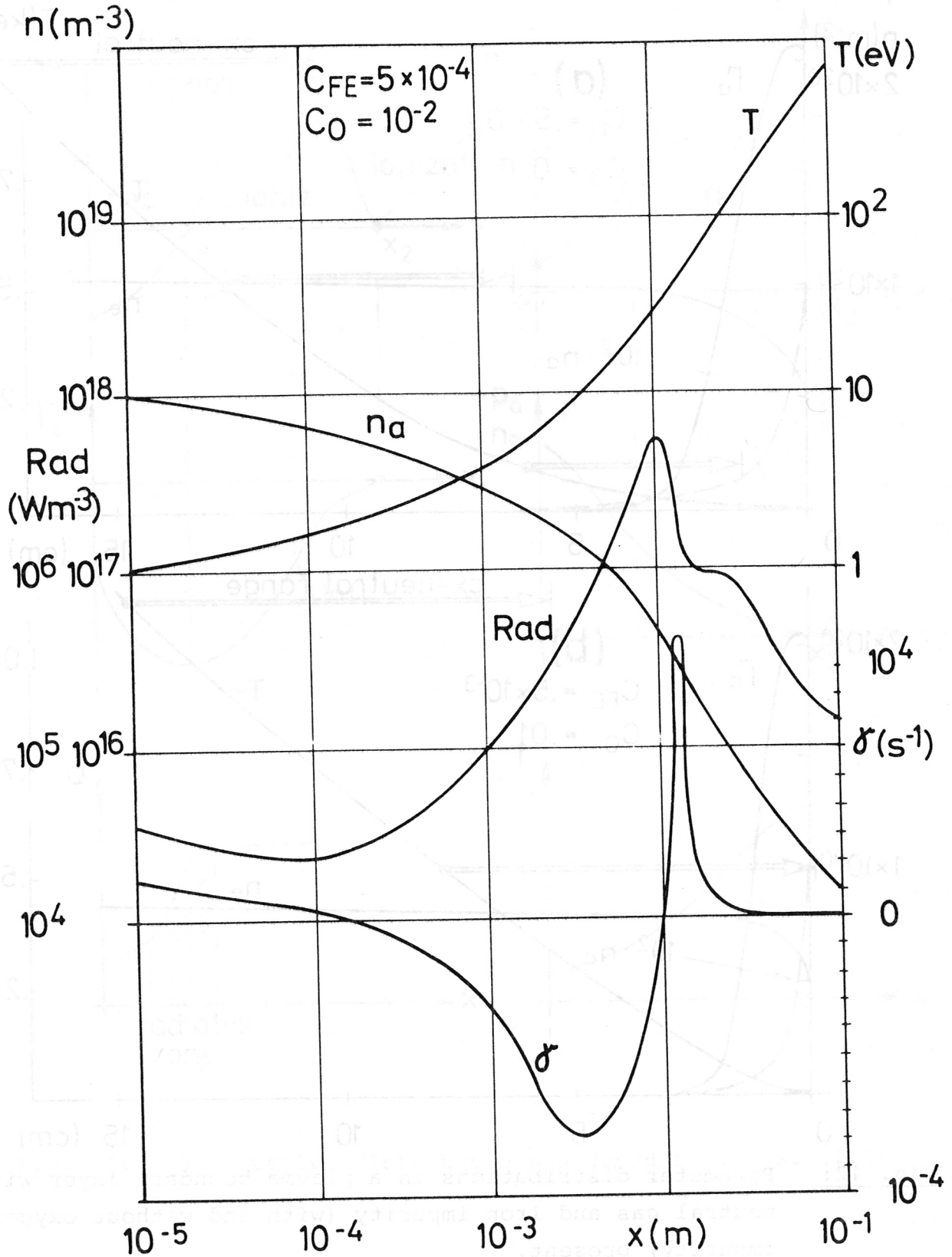


Fig. 13: Radiation loss and perturbation growth rate distributions for the case shown in Figure 12b.